Nat. Hazards Earth Syst. Sci., 10, 2599–2610, 2010
www.nat-hazards-earth-syst-sci.net/10/2599/2010/
doi:10.5194/nhess-10-2599-2010


Natural Hazards and Earth System Sciences

# Atmospheric pressure-wave bands around a cold front resulted in a meteotsunami in the East China Sea in February 2009

**K. Tanaka**

Department of Global Environmental Studies, Hiroshima Institute of Technology, 2-1-1, Miyake, Saeki-ku, Hiroshima 731-5193, Japan

Received: 6 April 2010 – Revised: 22 October 2010 – Accepted: 20 November 2010 – Published: 17 December 2010

**Abstract.** A meteotsunami hit southwest Kyushu on 25 February 2009, with an estimated maximum amplitude of 290 cm, which was higher than that recorded for the 1979 Nagasaki event. This study investigated mesoscale meteorological systems over the East China Sea during the time leading up to the February 2009 event using a Weather Research and Forecast model. The disturbance in the sea-level pressure originated from a gravity wave over southeastern China. The sea-level pressure disturbance observed and modelled over the East China Sea had its source over the southeastern China mountains and was then propagated by a jet stream toward western Japan with the help of both wave-duct and wave-CISK (conditional instability of the second kind) mechanisms. Two synoptic systems supported the momentum convergence and the formation of band-shaped unstable layers in the mid-troposphere. The high-latitude trough extended from eastern Siberia and there was subtropical high pressure over the western Pacific Ocean. The phase speed of the atmospheric wave was as high as 25–30 m s$^{-1}$, corresponding to the phase speed of long ocean waves on the East China Sea. Improvements in determining the amplitude and timing of the disturbance remain for future work.

## 1 Introduction

Meteotsunamis are long-period waves in the tsunami frequency band generated by a travelling atmospheric disturbance (Vilibić and Šepić, 2009). With high phase velocities and high amplitudes, meteotsunamis can be destructive in coastal areas (e.g., Monserrat et al., 2006; Haslett et al., 2009; Goring, 2009). In western Japan (Fig. 1), meteotsunamis are called *abiki*, which means "the dragging away of a fishing net" (Kakinuma et al., 2009).

According to a report by Shiga et al. (2007), meteotsunamis are recorded approximately five times per year on average, with some tidal observatories recording them more than ten times per year. The statistical record shows that the maximum amplitude of a meteotsunami has exceeded 100 cm for most of southern Kyushu. Until the 2009 event, the greatest amplitude for a meteotsunami in Japan was 279 cm in Nagasaki Bay, western Kyushu, on 31 March 1979.

There are many mechanisms that can create a meteotsunami source such as the occurrence of an extratropical cyclone (e.g., Goring, 2009), the passage of a typhoon or hurricane (excluding storm surges) (Shiga et al., 2007), the passage of a cold front (de Jong et al., 2003), a synoptic high-pressure system (Shiga et al., 2007), atmospheric pressure jumps (Akamatsu, 1982), and the propagation of low-troposphere gravity waves (Šepić et al., 2009a, b). However, these atmospheric sources have typical scales of a few hPa, equivalent to a few centimetres of sea-level change. Resonant effects occurring at the oceanic-atmospheric interface, such as those reported by Proudman (1929) or Greenspan (1956), may significantly amplify ocean waves reaching the coast (Monserrat et al., 2006; Rabinovich, 2009).

Hibiya and Kajiura (1982) conducted a numerical simulation using an idealized single pressure wave. They showed that the atmospheric pressure disturbance was amplified over the broad continental shelf region because of near-resonant coupling to the pressure disturbance and was also amplified at eigenperiods of the bay. Dotsenko and Mikashevskaya (2008) simulated the case of a baric front moving over the Black Sea in which the pressure distribution was given as a function of distance from the front. Vilibić et al. (2008) attempted to simulate the propagation of a meteotsunami by importing an observed atmospheric pressure disturbance and

*Correspondence to:* K. Tanaka
(k.tanaka.pb@cc.it-hiroshima.ac.jp)

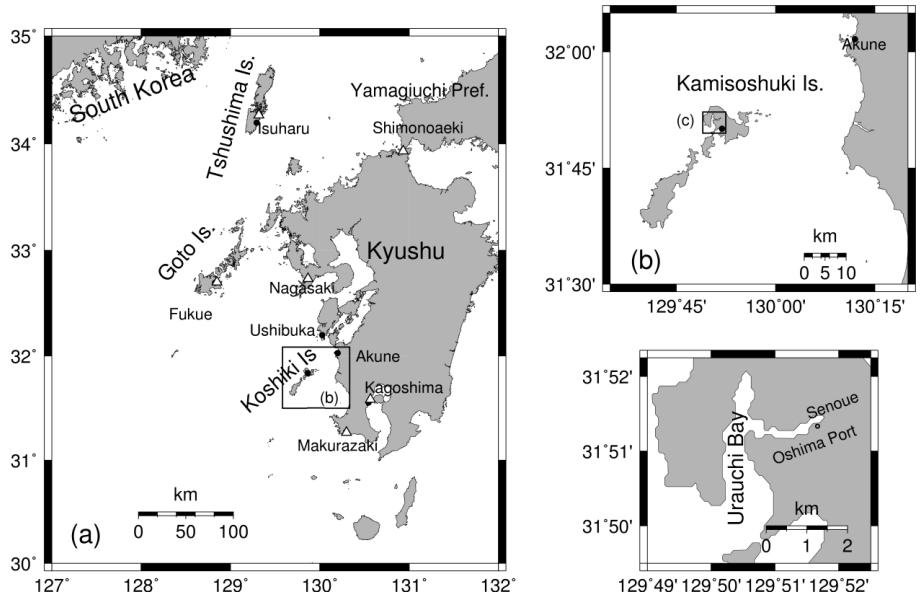


**Fig. 1.** Maps of the western Kyushu Islands **(a)**, Koshiki Islands **(b)**, and Urauchi Bay **(c)** of Kamikoshiki Island.

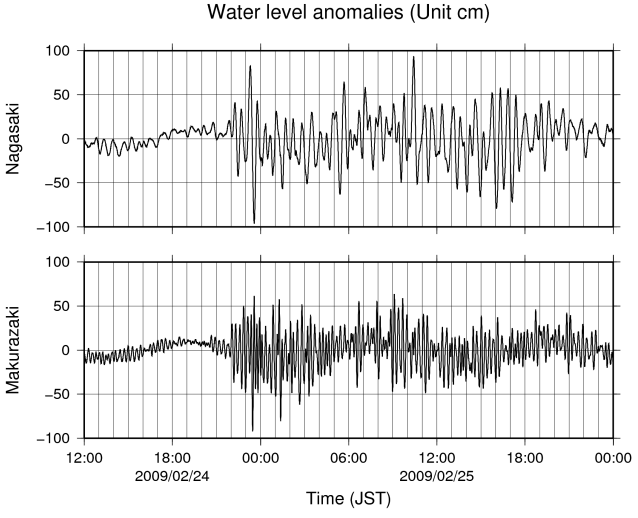


**Fig. 2.** Water-level anomalies observed at Nagasaki and Makurazaki. Original data were provided by the Nagasaki Meteorological Bureau and the Japan Meteorological Agency.

pointed out the importance of the fine spatial resolution of bathymetric data. Field studies have also revealed a high correlation between the pressure disturbance and sea-level oscillations (Rabinovich and Monserrat, 1996).

With respect to a pressure perturbation that induces a meteotsunami, it is known that there are basically two mechanisms that can enable a generated gravity wave to maintain or recover its energy while propagating away from the source region at long scales, i.e., wave-duct (e.g., Monserrat and Thorpe, 1996) and wave-CISK (conditional instability of the second kind) mechanisms (e.g., Belušić et al., 2007). Belušić et al. (2007) applied a mesoscale meteorological model to reproduce a meteotsunami event over the Adriatic Sea and proved that the wave-CISK mechanism may efficiently preserve the energy of an atmospheric disturbance over a large distance.

This study investigated the causal mechanism of an atmospheric pressure wave using a mesoscale meteorological forecast model. On 25 February 2009, a meteotsunami with the largest amplitude yet recorded landed in the Koshiki Islands west of Kyushu. In this event, the stationary front and the low-pressure system related to the pressure wave evolved in the East China Sea. The event is briefly overviewed before the numerical simulation is presented.

## 2 Overview of the meteotsunami event in February 2009

### 2.1 Meteotsunami event

Long-wave oscillations began on the night of 24 February 2009 over the entire western coast of Kyushu. Table 1 lists the maximum amplitudes recorded at the tidal observatories of the Japan Meteorological Agency (JMA), Japan Coast Guard and Geographical Survey Institute. The maximum amplitude exceeded 100 cm at Nagasaki, Makurazaki and Nakanoshima (see the locations in Fig. 1). Figure 2 shows the water-level anomalies observed at Nagasaki and Makurazaki, provided by the Nagasaki Meteorological Bureau and Japan Meteorological Society. The oscillations began to increase at 22:00 Japan Standard Time (JST) at both Nagasaki and Makurazaki. The maximum anomaly at Nagasaki

**Table 1.** Record of secondary oscillations observed in western Japan, reported by the Nagasaki, Marine Observatory et al. (2009).

| Station | Max. amp. (cm) | Period (min) | Time of recording (JST) | Max. water level (cm) | Time of recording (JST) |
|---|---|---|---|---|---|
| Fukue | 81 | 19 | 23:19, 24 Feb | 121 | 10:25, 25 Feb |
| Nagasaki | 157 | 29 | 23:34, 24 Feb | 174 | 10:25, 25 Feb |
| Makurazaki | 141 | 12 | 23:27, 24 Feb | 94 | 07:55, 25 Feb |
| Tanegashima | 85 | 14 | 02:07, 25 Feb | 159 | 06:22, 25 Feb |
| Nakanoshima | 153 | 5 | 09:46, 25 Feb | 118 | 08:11, 25 Feb |


**Fig. 3.** Sequence of photographs taken on 25 February 2009 at the Oshima port, Kamikoshiki Island, provided by the Kamikoshiki Branch Office, Satsuma-Sendai City.

**Fig. 4.** Photographs of dike damage at Urauchi Bay, Kamikoshiki Island, provided by T. Asano, Kagoshima University.

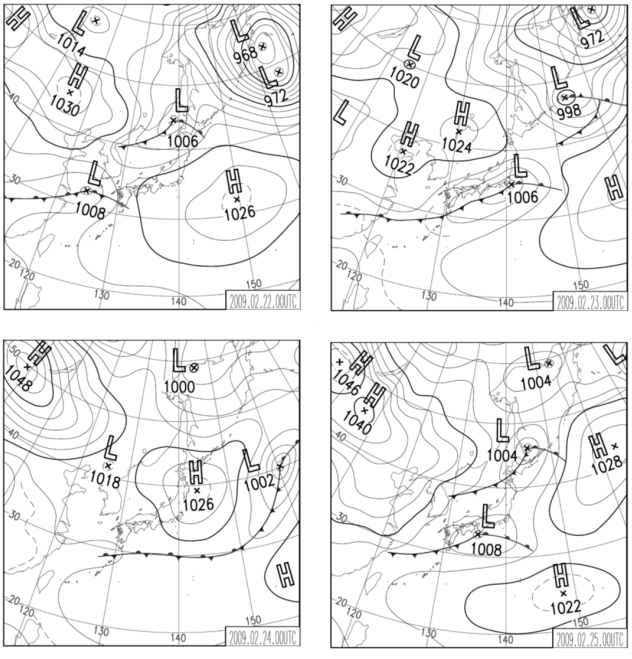


**Fig. 5.** Weather charts of the surface level from 22 February 2009 to 25 February 2009, provided by the Japan Meteorological Agency.

reached almost 1 m at 10:25 JST, corresponding to the maximum high-water level, as listed in Table 1.

On the morning of 25 February 2009, the oscillations increased and the water level was higher than the dike on the harbour at Urauchi Bay on Kamikoshiki Island (Fig. 1c). Urauchi Bay has a "T" shape, with a length of approximately 3.0 km in the latitudinal direction and a length of approximately 2.5 km in the longitudinal direction. Figure 3 is a sequence of photographs taken during the meteotsunami event. A fishing boat was capsized by the amplified oscillations (Fig. 3a) and its bow was damaged. The photographs in Fig. 3b–d show that the water level rose rapidly within the 12 min between 08:20 and 08:32 JST. At 08:30 JST, the water level reached the top of the dike (Fig. 3c), and the fishing-port area was partly flooded (Fig. 3d). Afterward, the water level decreased rapidly within 10 min (Fig. 3e and f).

According to a report by the Nagasaki Marine Observatory et al. (2009), 30 vessels had capsized and damaged in western Kyushu; 24 of these were located in the Koshikijima Islands. Eight residences were inundated below floor level in the Segami community along Urauchi Bay on Kamikoshiki Island. A field survey by Kakinuma et al. (2009) showed that the base of the Urauchi Bay dike was damaged and partly disintegrated, as shown in Fig. 4. The trail of flooding showed that the amplitude between 08:30 and 08:40 JST was as high as 290 cm, and the maximum high-water level was 68 cm higher than the benchmark level at the Oshima fishing port. The recorded maximum amplitude was higher than the previous record for western Kyushu (278 cm in Nagasaki on 31 March 1979).

The characteristics of the secondary oscillations in Urauchi Bay were examined by Yamashiro et al. (2009) by observing water levels and current speeds in October 2008 and March 2009. They found that the oscillation periods were 24.8–25.5 min for the first mode (a nodal mode at the mouth of the bay) and 7.2–12.6 min for the secondary mode (a nodal point at a junction).

## 2.2 Weather record

Surface weather charts provided by the JMA are shown in Fig. 5. On 22 February 2009, there was a low-pressure system moving eastward over the East China Sea. This low pressure brought a long and stationary cold front extending from the centre of the low-pressure area to mainland China (see the chart for 23 February). On 24 February, this low pressure moved eastward toward Japan (150° E), however, the western end of the front remained over the East China Sea. On the same day, a depression appeared over the northern part of the Korean Peninsula (42° N, 125° E); this depression then moved to northern Japan on 25 February. Another low-pressure system evolved over the East China Sea and moved along the Pacific coast of Japan. The stationary front remained over the East China Sea on 24 February, however, the cold front extended over the East China Sea on 25 February. A change in the front structure over the East China Sea seemed to generate the local pressure disturbance.

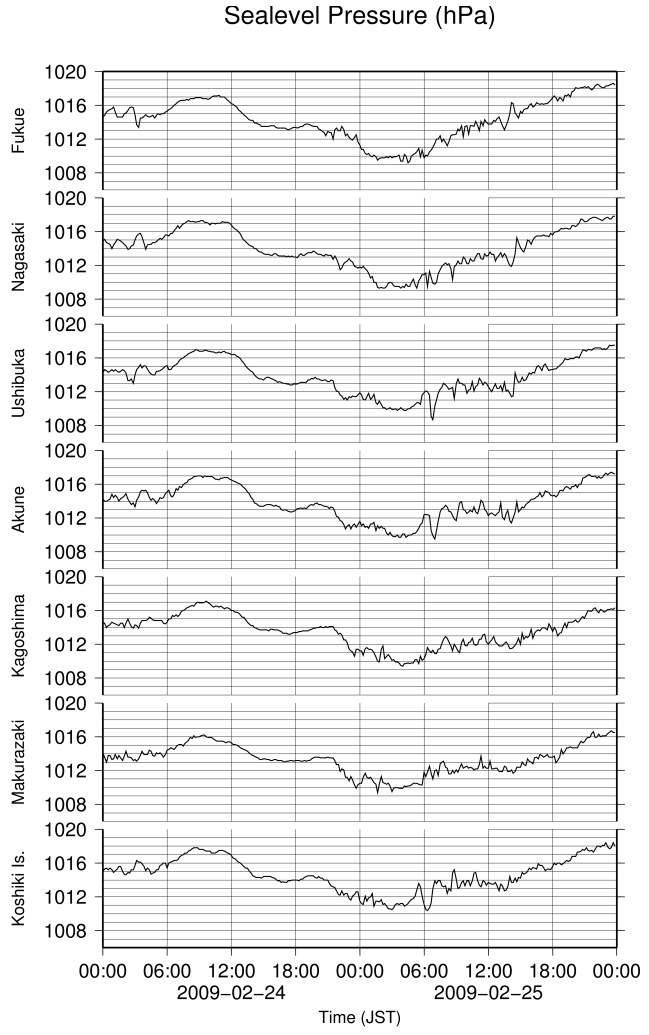


**Fig. 6.** Sea-level pressure observed in western Kyushu. All observations were by the Japan Meteorological Agency except for those at Kamikoshiki, which were by the Kamikoshiki Island branch of the Satsuma Sendai City Office.

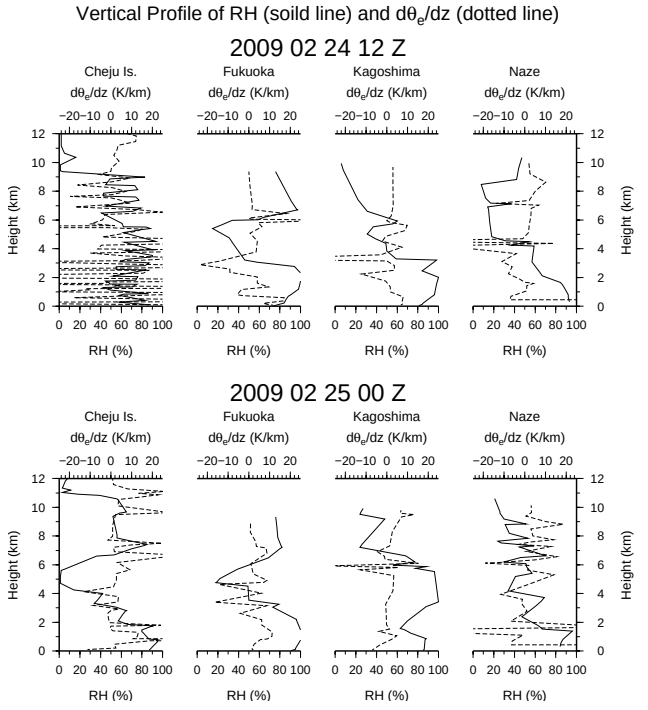


**Fig. 7.** Vertical profile of the relative humidity (solid line) and vertical gradient of the equivalent potential temperature $\theta_e$ (dotted line) obtained from rawinsonde observations.

Figure 6 shows the sea-level pressure at Nagasaki, where the data from Fukue, Ushibuka, Akune, Kagoshima and Makurazaki were observed at the Japan Meteorological Society at 10-min intervals. The sea-level pressure at Nakakoshiki in the Koshikijima Islands is also shown in Fig. 6. The sea-level pressure oscillated with an amplitude of 0.5–1 hPa. A pressure depression of 2 hPa was observed at both the Ushibuka (06:50 JST) and Akune (07:00 JST) observatories on the morning of 25 February. On Kamikoshiki Island, the pressure jumped by 2 hPa at 09:00 JST on 25 February. The surface pressure jumped by 3 hPa at Fukue between 13:40 and 14:10 JST, and similar pressure jumps were observed at Nagasaki and Ushibuka.

Figure 7 shows the vertical profiles of the relative humidity and the vertical equivalent potential-temperature gradient obtained from rawinsonde observations at four observatories: Cheju Island, South Korea (33.28° N 126.16° E), and Fukuoka, Kagoshima, and Naze (28.38° N 129.55° E). A dry air mass in the mid-troposphere (3–6 km above sea level (a.s.l.)) can be seen clearly in the Fukuoka and Kagoshima profiles at 12:00 UTC on 24 February, with the unstable layer located at the bottom of the dry air. At that time, the vertical profile of the relative humidity on Cheju Island fluctuated with a wavelength of approximately 500 m. The equivalent potential temperature on Cheju Island also fluctuated rapidly. At 00:00 UTC on 25 February, the dry air mass in the mid-troposphere can be seen in Fukuoka and Cheju Island and unstable layers can be seen between 3 km and 4 km a.s.l. However, in Kagoshima, the stratification in the low- and mid-troposphere (2–6 km a.s.l.) was neutral or weakly stable, with the dry air covering upwards of 6 km a.s.l. The convective-inhabitation index in Kagoshima was $-110\,\mathrm{J\,kg^{-1}}$ at the time.

The infrared imagery from the Multifunctional Transport Satellite (MTSAT) (Fig. 8) shows that a wave pattern of low-to-mid-level clouds, marked "A" in the upper panel, appeared over the middle of the East China Sea and approached the Kyushu Islands. The cloud-top level in the wave-pattern area (A) was not much higher than that in the surrounding regions. In the water-vapour channel of the MTSAT image (lower panel in Fig. 8), a darkish area, labelled "B", is seen near 30° N over the East China Sea, covering the wave-pattern area. The sinking of the dry air in that region capped the

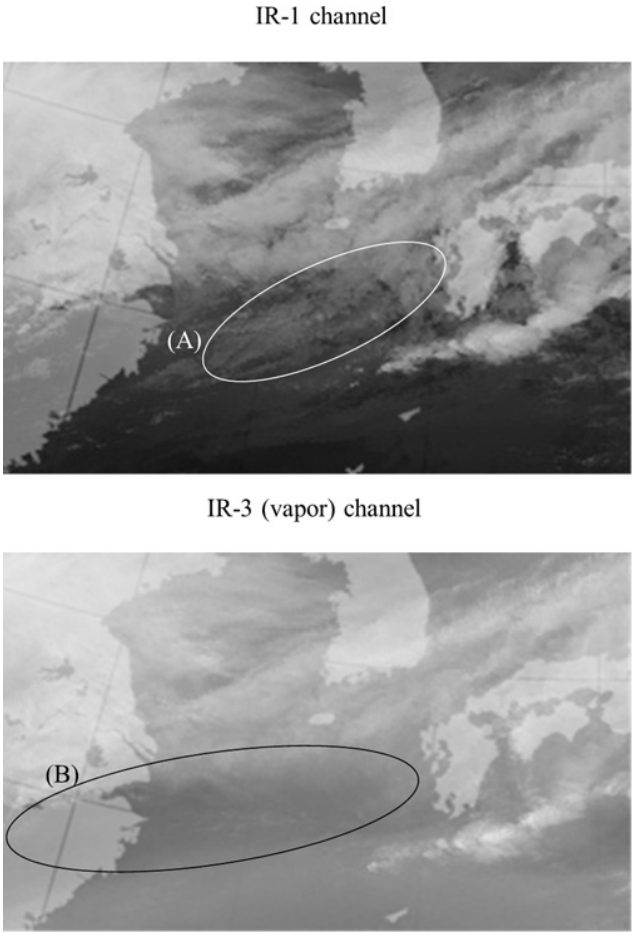


**Fig. 8.** MTSAT visible images over the East China Sea. A snapshot at 23:30 UTC on 24 February 2009.

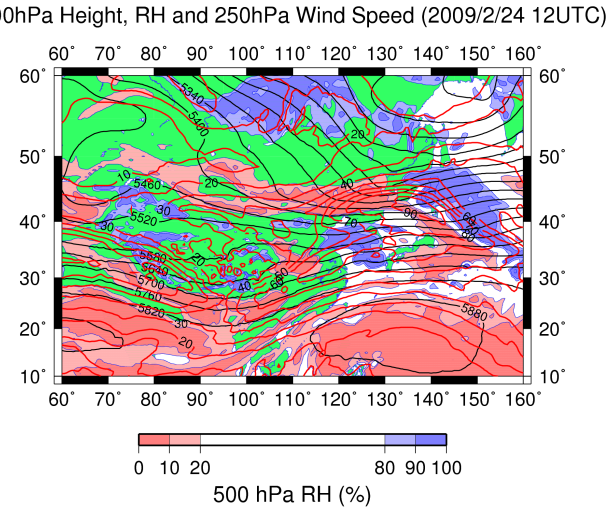


**Fig. 9.** Upper air field over the East Asia Region. Black solid lines indicate the geopotential height at 500 hPa. Red solid lines indicate the wind speed at the 250-hPa isobar. Colour bars show the relative humidity at the 500-hPa isobar.

convective clouds, corresponding to the vertical structure observed at Kagoshima in Fig. 7.

The upper air field in the East Asia region is plotted in Fig. 9 using the reanalysis data provided by the JMA Global Spectrum Model (Mizuta et al., 2006). Over Japan and mideastern China, the 250-hPa wind speed was stronger than $60\,\mathrm{m\,s^{-1}}$, whereas the subtropical and polar-front jets were close. The area between the 5700-m and 5820-m contour of the 500-hPa geopotential height, below the subtropical jets, jogged northward with high pressure over the Pacific Ocean, bringing dry air from the southeast.

## 3 Numerical simulation of meteorological fields

The Weather Research and Forecast (WRF) model is a numerical weather-prediction and atmospheric-simulation system designed for both research and operational applications (Skamarock et al., 2008). The development of the WRF model has been a multi-agency effort in building a next-generation mesoscale forecast-model and data-assimilation system with the aim of advancing the understanding and prediction of mesoscale weather and accelerating the transfer of research advances to practical applications. The WRF effort has been a collaborative partnership, principally among the National Centre for Atmospheric Research (NCAR), the National Oceanic and Atmospheric Administration (the National Centres for Environmental Prediction (NCEP) and the Forecast Systems Laboratory), the Air Force Weather Agency, the Naval Research Laboratory, the University of Oklahoma and the Federal Aviation Administration in the United States. The source code of the WRF model supports two solvers. One is the Advanced Research WRF (ARW), a research tool for simulation using a meteorological dataset or numerical experiments under ideal conditions such as a two-dimensional squall line, gravity wave, or sea breeze. The other is the Nonhydrostatic Mesoscale Model (NMM), which is designed for real-time prediction. The source code is open to users who register with the WRF community.

The WRF model can compute both large-scale motions (over 1000 km) and small-scale motions (under 1 km) using two-way nesting with multiple nests and nesting levels. Four-dimensional data assimilation (FDDA) is available using meteorological grid-point values combined with radiosonde/ground-observation data. Full physics options for land surface, planetary boundary layer, atmospheric and surface radiation as well as microphysics and cumulus convection are available.

There are four steps in simulating meteorological phenomena using WRF-ARW. The first step is to define the computational domain and map the projection and grid spacing. The second step is to interpolate grid point values provided by the NCEP, the JMA, the ECMWF (European Centre for Middle

Weather Forecast), and other sources to fit the grid spacing of the computational domain. These two steps are included in the WRF Preprocessing System. The third step is to set the initial conditions, boundary conditions and FDDA dataset by editing the namelist file. The fourth step is to run the main forecast programme. Because the output data have coordinates that follow the terrain, it is best for users to convert the data into a pressure-coordinate system, which can be done using a programme provided by NCAR. A flow chart for the application of the WRF-ARW system is provided in the user guide (Wang et al., 2010).

The computational domains in this study are shown in Fig. 10. The coarse domain (Domain 1) covers the entire East Asia region (80°–160° E, 13°–52° N), with a grid spacing of 50 km. The intermediate domain (Domain 2) covers the East China Plain and the middle-western Japan region (110°–140° E, 23°–42° N) with a grid spacing of 10 km. The fine domain (Domain 3) covers most of the East China Sea and Kyushu Island (118°–133° E, 28°–38° N) with a grid spacing of 2.5 km. All domains are projected into Mercator coordinates. The overall forecast duration was 48 h: from 12:00 UTC on 23 February 2009 to 12:00 UTC on 25 February 2009. The time steps selected for the three domains were 300, 60, and 15 s, respectively. Forecast gridded data were output every hour for Domain 1, every 30 min for Domain 2 and every 10 min for Domain 3. The author logged the surface meteorological variables of the Kamikoshiki Islands (31.849° N, 129.850° E; 43.5 m in the model topography) at each time step.

Because there was no snow in western Japan during the experimental period, it was not necessary to include the ramifications of snow physics. The cumulus scheme of Grell and Devenyi (2002) was applied for the subgrid scale of cumulus convection. Hence, WRF Simple Microphysics three-class simple ice schemes (Hong et al., 2004), which consider only three water phases, i.e., liquid, vapour and ice, were used in this study. Long-wave radiation (Mlawer et al., 2002; Dudhia, 1989). The Yonsei University scheme (Hong et al., 2006) was applied for atmospheric boundary-layer physics.

Reanalysis data, provided by the JMA, Global Spectrum Model (Mizuta et al., 2006), were used for generating initialization, boundary conditions and FDDA datasets. The daily sea-surface temperature dataset of the NCEP, with a horizontal resolution of 0.083°, was used for the surface conditions (Gemmill et al., 2007).

## 4 Results and discussion

### 4.1 Unstable layer in the mid-troposphere

Figure 11 shows the distribution of the minimum Richardson number ($Ri$) in the mid-troposphere (from 400 hPa to 700 hPa) over Domain 1. The shaded, unstable layer corresponds to $Ri < 0.25$. The Richardson number takes into consideration the atmospheric moisture content (Duran and Klemp, 1982) using the model outputs. The meteorological variables at 500 hPa (i.e., wind, geopotential height and relative humidity) are also plotted in Fig. 11. The unstable layer, induced by the atmospheric pressure disturbance, occurred in the coastal area of East China (119° E, 33° N) at 14:00 JST on 24 February 2009. In this area, the atmosphere was rather moist in the mid-troposphere, as evidenced by the 50-hPa relative humidity above 80%. A dry air mass was located upstream of the unstable layer at approximately 110° E 30° N, with a relative humidity less than 20%.

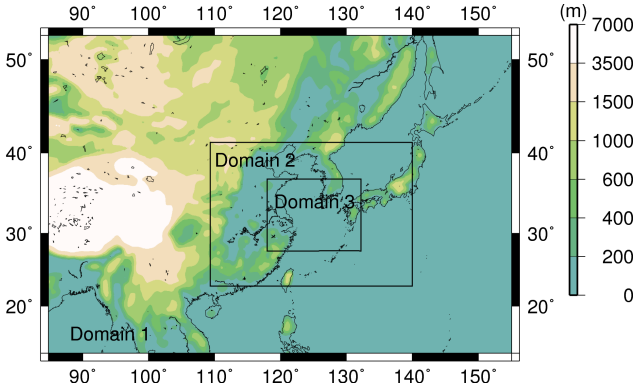


**Fig. 10.** Computational domain of this study. Colours indicate the topography of Domain 1.

As the time progressed, the unstable layer in East China expanded toward the East China Sea and then formed a narrow band with a latitudinal width of approximately 200–300 km. The dry air mass in the mid-troposphere moved northeast in the period between 14:00 JST and 21:00 JST on 24 February 2009. This dry air mass then turned slightly to the east, steered by the trough extending from east Siberia, near 35° N latitude, over the East China Sea. The dry air mass finally settled to the north of the unstable band. Hence, the unstable layer over the East China Sea became wedged in between the two dry air masses: the northern air mass described above and the subtropical high-pressure mass over the western Pacific Ocean.

The vertical-longitude cross-section of the area surrounding the unstable layer over the Chinese coastal area are shown in Fig. 12, as seen by a snapshot at 03:00 JST on 25 February 2009, using the Domain 2 output. The cross-section of the vertical wind is also shown in the lower panel of Fig. 12, however, in this case it is limited to the horizontal region between 120°–130° E. At 03:00 JST, the surface cold front was located near 126° E and convective cells could be seen behind it (at 122°–126° E). Additionally, there was a wind shear along the isograms of the equivalent potential temperature of 290 K. The unstable layer, shown by the hatched areas in both the upper and lower panels, was located between 600 hPa and 800 hPa, ahead of the front system, and was as high as 500 hPa in the convective area (124°–125° E).

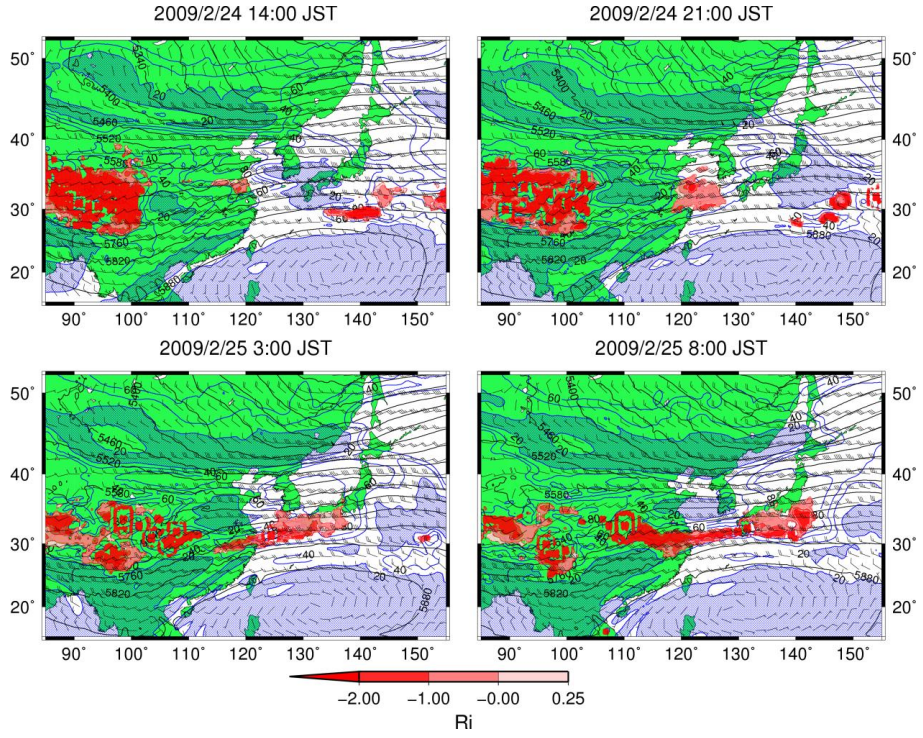


**Fig. 11.** Middle-troposphere instability in which the minimum bulk Richardson number was negative between the 400-hPa and 700-hPa layers, including a 500-hPa geopotential height, relative humidity (blue contour and the area of RH < 20% shaded by blue), and wind (each barb 10 m s$^{-1}$). The land areas are shown in green.

The unstable layer corresponded well to the relative humidity of 80–90% in the region between 120°–130° E. Updraft and downdraft couples were observed in the regions of 123°–126° E at 03:00 JST and 123°–127° E at 04:00 JST, respectively, resulting from the propagation of gravity waves from the mountainous areas of southeast China (see the topographic map in Fig. 10). The phase speed of the wave was estimated at 25–30 m s$^{-1}$ in the easterly direction and a wind direction of 240°–270°, as shown in Fig. 12.

The data support the implication of both the wave-duct and the wave-CISK mechanisms in the propagation of the gravity wave from southeastern China to western Japan. The presence of the wave duct requires an unstable layer ($Ri < 0.25$) in the upper layer that includes a critical (or steering) level (e.g., Belušić et al., 2007; Lindzen and Tang, 1976). The estimated phase speed reported above was as high as the mean wind speed of 700–600 hPa level inside the unstable sublayer. The wave-CISK mechanism denotes the coupling between the gravity wave and convection, where the convergence associated with the gravity wave forces the moist convection while convective heating provides the energy for the wave (Belušić et al., 2007; Lindzen, 1974). The trough extended from east Siberia and the subtropical high-pressure system generated the latitudinal convergence over the area of the unstable mid-troposphere.

### 4.2 Atmospheric pressure disturbance

The surface pressure over the middle of the East China Sea (Domain 3) is shown in Fig. 13, which also shows the divergence of the surface wind. The centre of the surface low pressure appeared near Cheju Island at 21:00 JST on 24 February 2009 and the disturbance in the sea-level pressure can be seen near the coastal area of Shanghai, China. The band of pressure disturbance propagated to Kyushu Island, moving the cold front with the low surface surface, corresponding to the region of the mid-troposphere unstable layer shown in Fig. 11. The wavelength of the pressure disturbance ranged from 30–100 km, as seen in the coupling of the updraft and downdraft in Fig. 12. Although the horizontal convergence and divergence of surface wind were strong inside the pressure-wave band, the wind speed itself was not high. The mean wind speed ranged from 5–10 m s$^{-1}$ in the NNW direction. The wave band began to split from the cold front at approximately 06:00 JST on 25 February, and the disturbance gradually decreased.

A close-up of the sea-surface wind and pressure in the west Kyushu coastal area is shown in Fig. 14. A convergence band with an intensity over $500 \times 10^{-6}$ s$^{-1}$ can be seen in the line from 128° E 31° N to 130° E 32° N, corresponding to the cold front at sea level. A high-pressure anomaly, marked "Q", moved northeast, along with the surface-wind convergence.

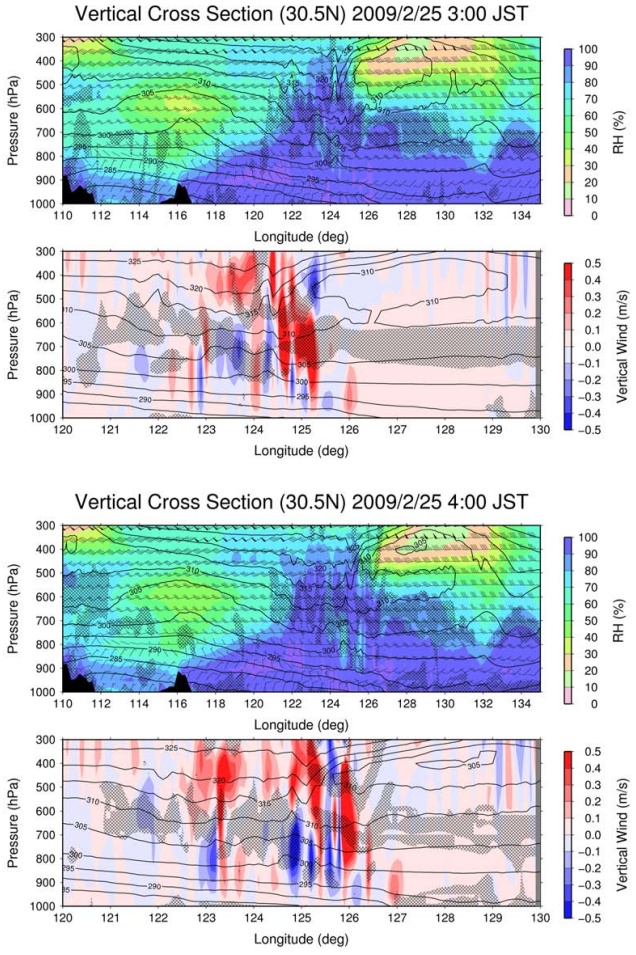


**Fig. 12.** Vertical-longitude cross-section of atmospheric variables at 30.5° N. The upper panel shows the relative humidity (colour), horizontal wind (each barb 10 m s$^{-1}$), equivalent potential temperature (black contour with an interval of 5°) and the unstable layer (shaded) with a negative bulk Richardson number. The lower panel shows the vertical wind speed (colour), equivalent potential temperature, and the unstable layer.

A branch of the surface-wind convergence can be seen to the east of the anomaly. Comparing the snapshots at 05:30 and 05:50, the anomaly and the convergence branch moved 0.35° to the east in 20 min, i.e., at approximately 27 m s$^{-1}$.

According to terrain data such as ETOPO1 obtained by the National Oceanic and Atmospheric Administration (Amante and Eakins, 2009), the depth of the targeted area is 60–150 m, except between 128.0° E and 129.5° E, where the depth is as great as 700 m. The phase velocity of the ocean long wave was estimated from the depth to be 25–35 m s$^{-1}$. Hence, the propagation velocity of the atmospheric pressure-wave band was nearly as high as the phase velocity of the ocean long wave.

Figure 15 shows the time series of sea-level pressure measurements at Koshiki Island. The increase in pressure at approximately 06:00 JST on 25 February is evident in both the computed and observed curves. The computation resulted in the pressure oscillations beginning just before the pressure jump, however, observations indicated that the oscillation of the sea-level pressure began at 21:00 JST on 24 February, ahead of the front system. The computed result was rather smoother than the 10-min observed record. It was likely that the computed result introduced a delay in the variation of the sea-level pressure of approximately 2–3 h before the pressure jump. The root-mean-square error of the computed sea-level pressure, taking 10-min averages, was 1.25 hPa throughout the forecast period and 1.0 hPa during the period of 03:00–21:00 JST on 25 February. This value was not terribly inaccurate in the overall computation, however, it was as high as the pressure disturbance.

Applying continuous wavelet analysis (Torrence and Compo, 1998) to the pressure-fluctuation data yielded the results presented in Fig. 16. Notice that the wavelet spectra are normalized by the maximum spectrum intensity for both the model and observation. The peak pattern related to the pressure jump at approximately 06:00 on 25 February was well matched in the simulation, with a period of 50–100 min. A peak at approximately 09:00 on 25 February was also found in both the model calculations and the 10-min observations. The peak period at 09:00 was approximately 25–35 min, which is nearly equal to the eigenoscillation period of the Urauchi bay. Although the peak appeared at 01:00 on 25 February in the observations, such a peak did not appear in the model. Conversely, the peak of the pressure fluctuation can be seen at approximately 18:00 JST in the model, yet this peak was not seen in the observations.

As the above results indicate, the propagation of the pressure disturbance along the cold front of the low-pressure system was well simulated. However, the pressure disturbance of another area inside the low-pressure system seen in the observations was not duplicated. Two factors may have affected the accuracy of the numerical simulation: the reanalysis dataset used in this study and the convective intensity including the microphysics. Both will be improved as the numerical model is further developed.

## 5 Conclusions

A numerical study was conducted on the meteorological status of the meteotsunami event that occurred in February 2009. A large pressure-wave band was found over the middle of the East China Sea, just to the north of the cold front of the surface low-pressure system. The pressure bands moved eastward and hit the Koshiki Islands, corresponding to the meteotsunami on the same day. The origin of the pressure-wave band was a gravity wave in middle-eastern China, as seen by the unstable layer in the middle troposphere. The subtropical high over the western Pacific Ocean and the Tibetan plateau played an important role in the evolution of the

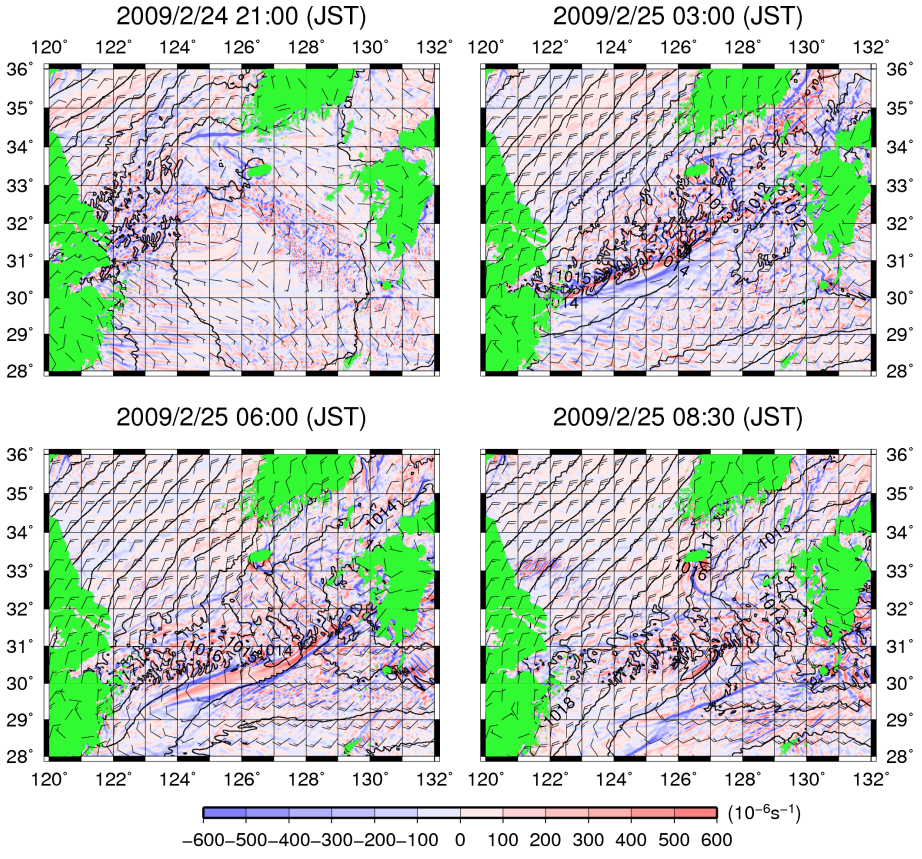


**Fig. 13.** Computed surface pressure (contour interval: 1 hPa) and divergence of the surface 10-m wind (colour scale). Wind barbs indicate $5\,\mathrm{m\,s^{-1}}$.

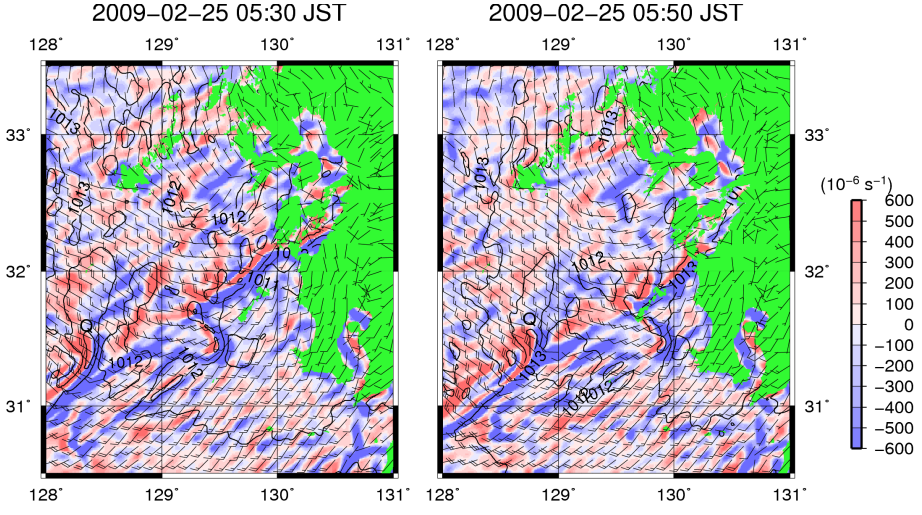


**Fig. 14.** Similar to Fig. 13, but the plotted area is limited to the coastal area of western Kyushu.

wave-CISK mechanism by transporting the dry air mass surrounding the unstable layer. The propagation speed of the atmospheric wave was 25–30 $\mathrm{m\,s^{-1}}$, corresponding to the phase velocity of the ocean long wave over the East China Sea. After removing the pressure variation with large-scale motion, the period of the surface pressure fluctuation was determined to be 10–100 min.

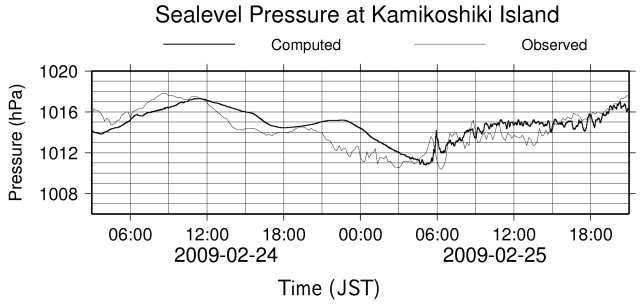


**Fig. 15.** Time series of the computed sea-level pressure.

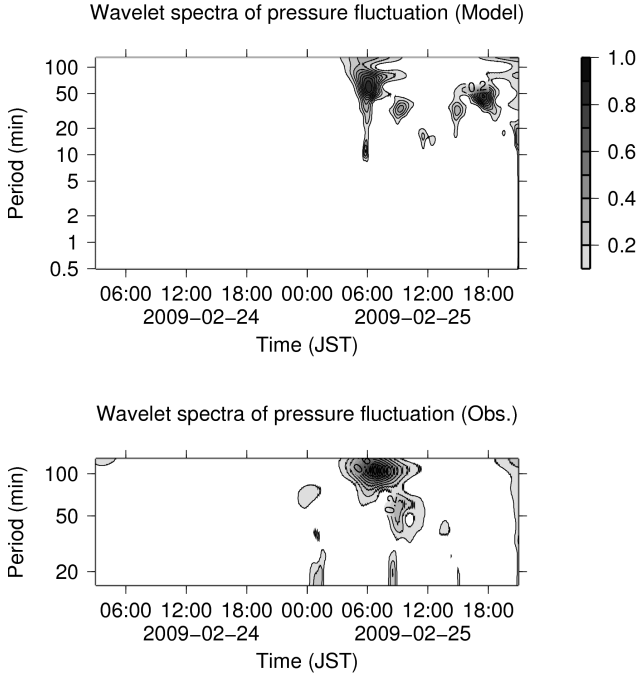


**Fig. 16.** Continuous wavelet spectra of the pressure disturbance, normalized to the maximum spectrum intensity.

An up-to-date meteorological model, meteorological-data product and computer can resolve the structure of a pressure oscillation that induces a meteotsunami to a considerable extent. However, in this model there remains insufficient accuracy for the wave intensity and pressure depression at the meso-$\gamma$ scale for coupling to ocean models. Further development of the convective process in the nonhydrostatic meteorological model will improve the resolution of the intensity of the pressure-wave band.

A detailed measurement of the surface pressure is also necessary to determine if there is pressure oscillation with a period of several tens of minutes, i.e., close to the eigenoscillation of the bay. The observations of meteorological variables in Japan, such as pressure, wind and temperature, are recorded as 10-min data. Moreover, the resolution of the pressure is generally 0.1 hPa. To resolve a pressure oscillation that induces a meteotsunami, it is necessary to record data once every several seconds, as for tidal observations, with a resolution of 0.01 hPa. The author plans to measure the pressure oscillations in the coastal area of western Kyushu in a further study.

*Acknowledgements.* The author thanks the Satsuma-Sendai city office for providing observation records. The author also thanks Toshiyuki Asano at Kagoshima University for discussions concerning the meteotsunami event at Koshiki Island.

Edited by: S. Tinti
Reviewed by: two anonymous referees

## References

Akamatsu, H.: On seiches in Nagasaki Bay, Pap. Meteorol. Geophys., 33, 95–115, 1982.

Amante, C. and Eakins, B. W.: ETOPO1 1 arc-minute global relief model: Procedures, data sources and analysis, NOAA Technical Memorandum NESDIS NGDC-24, National Geophysical Data Center Marine Geology and Geophysics Division, Boulder, Colorado, March 2009, 25 pp., 2009.

Belušić, D., Grisogono, B., and Klaić, Z. B.: Atmospheric origin of the devastating coupled air-sea event in the east Adriatic, J. Geophys. Res., 112, D17111, doi:10.1029/2006JD008204, 2007.

de Jong, M. P. C., Holthuijsen, L. H., and Battjes, J. A.: Generation of seiches by cold fronts over the southern North Sea, J. Geophys. Res., 108, C43117, doi:10.1029/2002JC001422, 2003.

Dotsenko, S. F. and Miklashevskaya, N. A.: Generation of seiches by moving basic fronts in bound basins, Phys. Oceanogr., 18, 63–77, 2008.

Dudhia, J.: Numerical study of convection observed during the winter monsoon experiment using a mesoscale two-dimensional model, J. Atmos. Sci., 46, 3077–3107, 1989.

Duran, D. R. and Klemp, J. B.: On the effects of moisture on the Brunt-Väisälä frequency, J. Atmos. Sci., 369, 2152–2158, 1982.

Gemmill, W., Katz, B., and Li, X.: Daily real-time, global sea surface temperature- highresolution analysis: RTG_SST_HR, NOAA/NCEP, NWS/NCEP/MMAB Office Note Nr. 260, 39 pp., available online at http://polar.ncep.noaa.gov/sst/, 2007.

Goring, D. G.: Meteotsunami resulting from the propagation of synoptic-scale weather systems, Phys. Chem. Earth, 34, 1009–1015, 2009.

Greenspan, H. P.: The generation of edge waves by moving pressure disturbances, J. Fluid Mech., 1, 574–592, 1956.

Grell, G. and Devenyi, D.: A generalized approach to parameterizing convection combining ensemble and data assimilation techniques, Geophys. Res. Lett., 29, 1693, doi:10.1029/2002GL015311, 2002.

Haslett, S. K., Mellor, H. E., and Bryant, E. A.: Meteo-tsunami hazard associated with summer thunderstorms in the United Kingdom, Phys. Chem. Earth, 14, 1016–1022, 2009.

Hibiya, T. and Kajiura, K.: Origin of the Abiki phenomenon (a kind of seiche) in Nagasaki Bay, J. Ocean. Soc. Japan, 38, 172–182, 1982.

Hong, S. Y., Dudhia, J., and Chen, S.-H.: A Revised approach to ice microphysical processes for the bulk parameterization of clouds and precipitation, Mon. Weather Rev., 132, 103–120, 2004.

Hong, S. Y., Noh, Y., and Dudhia, J.: A new vertical diffusion package with explicit treatment of entrainment processes, Mon. Weather Rev., 134, 2318–2341, 2006.

Kakinuma, T., Asano, T., Inoue, T., Yamashiro, T., and Yasuda, K.: Survey of February 2009 abiki disaster in Urauchi bay, Kamikoshiki Island, Annual J. of Coastal Eng., Japan Soc. Civil Eng., B2-65, 1391–1395, 2009 (in Japanese).

Lindzen, R. S.: Wave-CISK in the tropics, J. Atmos. Sci., 31, 156–179, 1974.

Lindzen, R. S. and Tang, K.-K.: Banded conducting activity and ducted gravity waves, Mon. Weather Rev., 104, 1602–1617, 1976.

Mizuta, R., Oouchi, K., Yoshimura, H., Noda, A., Katayama, K., Yukimoto, S., Hosaka, M., Kusunoki, S., Kawai, H., and Nakagawa, M.: 20-km-Mesh Global Climate Simulation Using the GSM-JMA Model for Mean Climate States, J. Meteorol. Soc. Jpn., 84, 166–185, 2006.

Mlawer, E. J., Taubman, S. J., Brown, P. D., Iacono, M. J., and Clough, S. A.: Radiative transfer for inhomogeneous atmosphere: RRTM, a validated correlated-k model for the long-wave, J. Geophys. Res., 102, 16663–16682, 1997.

Monserrat, S. and Thorpe, A. J.: Use of duction theory in an observed case of gravity waves, J. Atmos. Sci., 53, 1724–1736, 1996.

Monserrat, S., Vilibić, I., and Rabinovich, A. B.: Meteotsunamis: atmospherically induced destructive ocean waves in the tsunami frequency band, Nat. Hazards Earth Syst. Sci., 6, 1035–1051, doi:10.5194/nhess-6-1035-2006, 2006.

Nagasaki Marine Observatory, Kagoshima Local Meteorological Observatory, and Kumamoto Local Meteorological Observatory: Report on field survey of secondary oscillation around the coastal area of west Kyushu from 24 to 28, 24 pp., February 2009.

Proudman, J.: The Effects on the sea of changes in atmospheric pressure, Geophys. J. Intl., 2, 197–209, 1929.

Rabinovich, A. B.: Seiches and harbour oscillations, in: Handbook of Coastal and Ocean Engineering, World Scientific, Singapore, 193–236, 2009.

Rabinovich, A. B. and Monserrat, S.: Meteorological tsunamis near the Balearic and Kuril Islands: descriptive and statistical analysis, Nat. Hazards, 13, 55–90, 1996.

Šepić, J., Vilibić, I., and Belušić, D.: Source of the 2007 Ist meteotsunami (Adriatic Sea), J. Geophs. Res., 114, C03016, doi:10.1029/2008JC005092, 2009a.

Šepić, J., Vilibić, I., and Monserrat, S.: Teleconnections between the Adriatic and Balearic meteotsunamis, Phys. Chem. Earth, 34, 928–937, 2009b.

Shiga, T., Ichikawa, M., Kusumoto, K., and Suzuki, H.: A statistical study on seiche around Kyushu and Satsunan Islands, Pap. Meteorol. Geophys., 74, S139–S162, 2007.

Skamarock, W. C., Klemp, J. B., Dudhia, J., Gill, D. O., Baker, D. M., Duda, M. G., Hunag, X. Y., Wang, W., and Powers, J. G.: A Description of the Advanced Research WRF Version 3, NCAR Techical Note TN-475+ STR, 113, 2008.

Torrence, C. and Compo, G. P.: A practical guide to wavelet analysis, B. Am. Meteorol. Soc., 79, 61–78, 1998.

Vilibić, I. and Šepić, J.: Destructive meteotsunamis along the eastern Adriatic coast: overview, Phys. Chem. Earth, 34, 904–917, 2009.

Vilibić, I., Monserrat, S., Rabinovich, A., and Mihanovic, H.: Numerical Modelling of the Destructive Meteotsunami of 15 June 2006 on the Coast of the Balearic Islands, Pure Appl. Geophys., 165, 2169–2195, 2008.

Wang, W., Bruyère, C., Duda, M., Dudhia, J., Gill, D., Lin, H.-C., Michalakes, J., Rizvi, S., and Zhang, S.: ARW Version 3 modeling system user guide, Mesoscale & Microscale Meteorology Division, National Center for Atmospheric Research, 312 pp., 2010.

Yamashiro, T., Yasuda, K., Kuboyama, T., Jyomoto, K., Kakinuma, T., and Asano, T.: Characteristics of secondary undulations in Urauchi Bay of Kamikoshiki Island, Annual J. Civil Eng. in Ocean, Japan Soc. Civil Eng., 25, 1365–1370, 2009 (in Japanese).